Anal. Bioanal. Electrochem., Vol. 17, No. 8, 2025, 662-676
https://www.doi.org/10.22034/abec.2026.733509

Analytical & Bioanalytical Electrochemistry

Full Paper

Hydrothermal Green Synthesis of rGO Incorporated with TiO_2-NiO-MnO_2 Nanocomposite for Sensor Materials

Diah Febryana,[1] Maulidiyah Maulidiyah,[2,*] Zul Arham,[3,5] Muhammad Zakir Muzakkar,[2] Alimin Alimin,[2] Muhammad Nurdin,[2] Irwan Irwan,[4] Fharaz Jhanizza,[3] and Fadil Arham[5]

[1]Magister Student, Study Program of Chemistry Science, Post Graduate School, Universitas Halu Oleo, Kendari 93232- Southeast Sulawesi, Indonesia
[2]Department of Chemistry, Faculty of Mathematics and Natural Sciences, Universitas Halu Oleo, Jl. H.E.A. Mokodompit Kampus Baru Anduonohu, Kendari 93232 – Southeast Sulawesi, Indonesia
[3]Department of Mathematics and Natural Sciences, Institute Agama Islam Negeri (IAIN), Kendari, Southeast Sulawesi 93563, Indonesia
[4]Department of Pharmacy, Faculty of Sciences and Technology, Institut Teknologi dan Kesehatan Avicenna, Kendari 93117, Southeast Sulawesi, Indonesia
[5]Research Center of Nickel and Nano Energy, Institut Agama Islam Negeri (IAIN), Kendari, Southeast Sulawesi 93116, Indonesia

*Corresponding Author, Tel.: +6281388327118
E-Mail: maulid06@yahoo.com

Received: 16 July 2025 / Received in revised form: 27 July 2025 / Accepted: 28 July 2025 / Published online: 31 December 2025

Abstract- In this study, a novel voltammetric sensor for the detection of bisphenol A (BPA) was developed using a reduced graphene oxide (rGO) electrode incorporated with a TiO_2-NiO-MnO_2 nanocomposite (rGO/TNM). The TNM nanocomposite was synthesized via a hydrothermal method, and its integration with rGO improved the sensor's electrochemical performance by enhancing conductivity, surface area, and active sites. Characterization of the TNM nanocomposite using X-ray diffraction (XRD) confirmed the formation of distinct anatase TiO_2, γ-MnO_2, and NiO phases, each contributing to the synergistic enhancement of electrocatalytic properties. Fourier-transform infrared (FTIR) spectroscopy indicated the presence of characteristic metal-oxygen bonds, validating the successful formation of the TNM nanocomposite. Scanning electron microscopy (SEM) revealed a highly uniform and porous morphology with well-dispersed nanoparticles, ideal for maximizing electron transfer. Elemental analysis through energy-dispersive X-ray (EDX) spectroscopy further confirmed the

purity and composition of the nanocomposite. Under optimal conditions, the linear range of the rGO/TNM electrode by CV measurement was from 0.1 $\mu g.L^{-1}$ to 1.0 $\mu g.L^{-1}$, with a sensitivity and limit of detection (LOD) at 0.01094 $\mu g.L^{-1}$. These results make the developed sensor a promising candidate for environmental monitoring of BPA and highlight the potential of nanocomposite-modified electrodes in advancing electrochemical sensor technology.

Keywords- Reduced graphene oxide; TiO_2-NiO-MnO_2; Nanocomposite; Voltammetric sensor; Bisphenol A

1. INTRODUCTION

Recently, the chemical compound Bisphenol A (BPA) has frequently been associated with endocrine disruptors, posing significant environmental and health risks. BPA has been used since the 1950s to produce polycarbonate plastics and epoxy resins [1]. Besides serving as an adhesive, epoxy is also used as a lining or coating in food or beverage cans [2]. Disruptions to the endocrine system can lead to conditions such as cancer, diabetes mellitus, hypertension, and more [3]. Additionally, BPA can cause fertility issues, mental disorders, and developmental delays in children. According to the European Food Safety Authority (EFSA), the threshold limit for BPA release is set at less than 0.05 ppm [4,5]. Therefore, accurate and reliable detection of BPA is crucial to prevent its harmful effects.

Currently, various traditional methods for BPA detection have been widely used, such as liquid chromatography techniques [6], chromatography-mass spectrometry [7], fluorescence polarization immuno assay (FPIA) [8], enzyme-linked immunosorbent assays (ELISA) [9], lateral flow immunoassay (LFIA) [10], and others. However, these methods tend to be complex, require expensive equipment, and rely on trained professionals. Biomolecule detection typically depends on natural diffusion processes, which are often slow and less ideal for rapid BPA detection. For instance, Kumar et al. [11] developed a technique to measure BPA concentrations in five brands of canned soft drinks and bottled water using liquid chromatography coupled with tandem mass spectrometry, but this process takes considerable time. Additionally, Jia et al. [13] also demonstrated an innovative colorimetric biosensor based on CeO_2@ZIF-8/Apt composites; however, this method still requires too much time for rapid detection applications. Recently, various types of electrochemical sensors have gained increasing attention due to their numerous advantages.

Electrochemical methods, such as cyclic voltammetry, are increasingly favored for detection processes due to their high sensitivity, ease of application, minimal solvent requirements, relatively low cost, and the lack of need for specialized expertise [12–14]. In practice, this technique requires three electrodes: a working electrode, a counter electrode, and a reference electrode, with the working electrode playing a critical role in the detection of analyte compounds [15]. In many cases, it is essential to modify the surface of the working electrode to enhance peak currents and facilitate the redox reactions of the analyte molecules. Therefore, electrode material modification is crucial for improving sensor performance in

terms of sensitivity, selectivity, and reproducibility [16–18]. The working electrode can be modified through physical and chemical approaches, including the use of composite materials, nanomaterials, and polymers, which have been proven effective in enhancing the performance of electrochemical sensors [19,20].

Reduced Graphene oxide (rGO) can be modified through both chemical and physical approaches. Hidayat et al. [21] developed a BPA sensor by combining a carbon paste electrode (CPE) with a TiO_2/rGO composite. This study demonstrated that the BPA sensing process involves an irreversible reaction controlled by diffusion currents. The sensor also exhibited an outstanding detection limit of 0.08 μM. Similarly, Buledi et al. [22] modified the GPE by integrating reduced graphene oxide with NiO-ZnO nanoparticles (rGO/NiO-ZnO) for the detection of BPA in mineral and tap water. The synergistic effect of rGO and NiO-ZnO resulted in superior conductivity with an ohmic resistance value of 412 Ω. This sensor achieved effective recovery for monitoring various levels of BPA in drinking water and tap water samples. Previously, Lou et al. [23] reported that MnO_2 microspheres modified with carbon ion liquid exhibited enhanced stability due to the role of MnO_2 nanoparticles in improving electron transfer during the BPA monitoring process. Similarly, Nasehi et al. [24] modified multiwall carbon nanotubes (MWCNTs) with TiO_2-ion liquid for BPA detection in soft drinks. The study showed that TiO_2 nanoparticles were effective in facilitating electron transport in the working electrode. This phenomenon highlights that nanomaterials are highly effective in enhancing electrode performance, owing to their large surface area and high surface-to-volume ratio.

In this work, we successfully synthesized TiO_2-NiO-MnO_2 (TNM) bimetallic nanocomposites through a stainless steel-lined autoclave hydrothermal method by simultaneously adding three types of metal ions. Variations in the molar ratio between Ti, Ni, and Mn ions were also conducted in this study. The TNM bimetallic nanocomposites were then incorporated into a conductive material, namely reduced Graphene Oxide (rGO), to maximize and enhance the performance, conductivity, surface area, and active sites of the rGO [25]. For the first time, we report the development of a new electrode based on TNM bimetallic incorporated with rGO (rGO/TNM) for high-sensitivity BPA detection. This bimetallic-based sensor offers broad potential applications in modern electrochemical sensor technology.

2. EXPERIMENTAL SECTION

2.1. Apparatus

The crystal phase of nanocomposite materials was investigated using X-ray diffraction (XRD, UltimaIV, Rigaku, Japan), while their surface morphology was analyzed by scanning electron microscopy (SEM, Jeol JSM-7001F, Tokyo-Japan). Fourier Transform Infrared (FTIR) was employed to characterize the functional group nanocomposite materials used for electrode modification. Electrochemical experiments were conducted using a Potentiostat

DY2100B. A three-electrode system was utilized for electrochemical measurements, comprising a graphene paste electrode (GPE, 3 mm) or its modified version as the working electrode, a platinum wire as the counter electrode, and an Ag/AgCl as the reference.

2.2. Synthesis of rGO Nanomaterials

The synthesis of rGO nanomaterials was conducted based on a modified Hummers' method. Briefly, 0.4 grams of graphite oxide (GO) was dispersed in 100 mL of distilled water and stirred for 4 hours. The resulting suspension was then transferred into a Teflon-lined autoclave and heated at 160 °C for 12 hours. After the hydrothermal treatment, the obtained GO was dried at 105 °C for 3 hours and subsequently calcined at 500 °C for 1 hour.

2.3. Synthesis of TNM Nanocomposite

The synthesis of the TNM nanocomposite was initially by weighing 1 gram of TiO_2 powder, which was then added to 25 mL of 0.5 M $MnCl_2.4H_2O$ solution while stirring for 20 minutes at 50ºC. This step is followed by the addition of 25 mL of 0.5 M $NiSO_4.4H_2O$ solution with stirring for the same duration. The mixed solution is then subjected to microwave irradiation at 600 watts for 5 minutes. After cooling, the mixture is transferred into a hydrothermal Teflon-lined autoclave and heated at 180ºC for 3 hours. Upon completion of the reaction, 7.5 mL of 5 M NaOH solution is gradually added until a gel forms. In the final step, the sample is calcined at 500ºC for 1 hour, resulting in a yellowish-brown TNM powder.

2.4. Fabrication of rGO/TNM Working Electrode

Through the development of our procedure previously, 0.7 g of rGO/TNM nanocomposite was placed into a glass vial containing 0.3 g of paraffin oil. The mixture was then stirred uniformly using a magnetic stirrer at 80°C for 15 minutes, resulting in the formation of a homogeneous rGO/TNM paste. This paste underwent characterization via XRD, SEM-EDS, and FTIR techniques. Subsequently, the prepared paste was loaded into a glass tube with an approximate inner diameter of 0.4 mm, which functioned as the electrode casing. The material was compacted mechanically to shape the electrode, after which the electrode surface was polished using sandpaper. Finally, a copper wire was attached to establish electrical contact.

2.5. Performance Test of Electrodes in BPA Detection

In voltammetry sensors, the rGO/TNM was used as the working electrode, connected with Ag/AgCl (reference electrode) and platinum wire (counter electrode) in a Potentiostat circuit utilizing the Cyclic Voltammetry (CV) method. In short, the voltammetric cell contains a test solution of 10 µM BPA and 0.01 M phosphate buffer, and measurements are conducted with a scan rate of 0.1 V/s, within a potential range of -0.8 V to 0.8 V. The performance test and

analytical parameters of the rGO/TNM electrode include the following evaluations: the effect of supporting electrolyte, pH influence, buffer influence, linear detection range, detection limit, repeatability and reproducibility, selectivity, electrode lifespan, and real sample analysis.

3. RESULTS AND DISCUSSION

3.1. XRD Analysis

The phase composition and purity of the TNM nanocomposite were examined using XRD, as illustrated in Figure 1. The presence of sharp peaks in the diffraction pattern indicates that the nanocomposite exhibits high crystallinity. Diffraction peaks appearing at 2θ values of 25.1°, 38.9°, 49.6°, 53.4°, 54.6°, and 65.3° are attributed to the (101), (004), (200), (105), (211), and (204) crystal planes of the anatase TiO_2 phase, in accordance with JCPDS card No. 84-1286. [26]. The presence of the anatase phase is crucial, as anatase TiO_2 is known for its superior photocatalytic and electrocatalytic properties compared to other phases. Additionally, the diffraction peaks at 2θ = 37.8° and 58.7° are associated with the (031) and (106) crystal planes of γ-MnO_2 (Figure 1c), corresponding to JCPDS No. 00-014-0644 [27]. The presence of γ-MnO_2 is crucial as this material is known for its high oxidative capacity, which enhances the sensor's capability in electrochemical detection processes [28]. Meanwhile, the peaks at 61.4° and 68.2° correspond to the (220) and (002) crystal planes of the β-MnO_2 phase, which also exhibits significant electrocatalytic activity (JCPDS No. 24-0735) [29]. Meanwhile, the NiO phase shows a characteristic diffraction peak at 2θ = 62.7°, which corresponds to the (220) crystal plane of the cubic crystal structure of NiO, as per JCPDS No. 47–1049 [30]. NiO, with its p-type semiconductor properties, is known for its good catalytic activity in redox reactions, and its ability to enhance electron transfer in electrochemical systems [31].

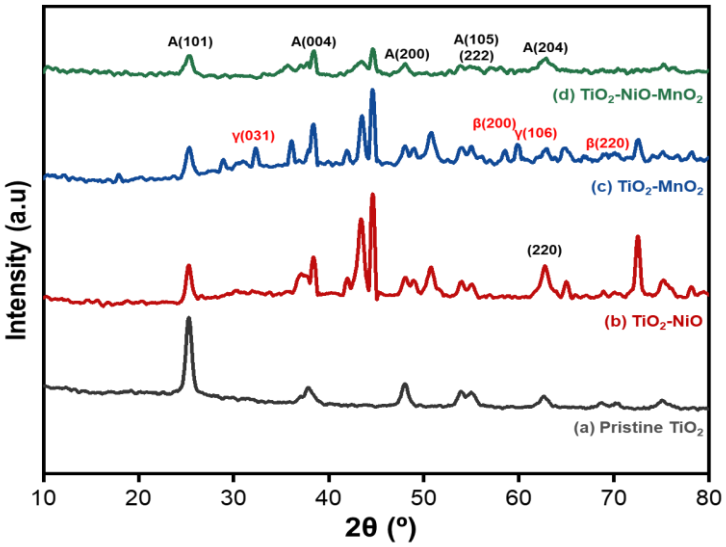

Figure 1. XRD pattern of (a) pristine TiO_2, (b) TiO_2-NiO, (c) TiO_2-MnO_2 and (d) TiO_2-NiO-MnO_2

The presence of the NiO phase in this nanocomposite plays a crucial role in accelerating the rate of electrocatalytic reactions, particularly in detecting target molecules, as NiO improves conductivity and increases the active surface area. The presence of various crystal phases (anatase TiO_2, γ-MnO_2, β-MnO_2, and NiO) within this nanocomposite creates a synergistic effect that enhances the electrochemical activity of the electrode, resulting in improved sensor performance for detecting target compounds.

3.2. FTIR Analysis

The Fourier Transform Infrared (FTIR) spectroscopy analysis was conducted to identify the functional groups present in the TNM nanocomposite and to confirm the successful formation of metal oxide bonds. The FT-IR spectrum of the TNM nanocomposite was measured over the wavenumber range of 500 cm^{-1} to 4000 cm^{-1}, as illustrated in Figure 2. The peak is broad and sharp at 3400 cm^{-1}- and 1620 cm^{-1} is attributed to the O-H stretching vibrations of adsorbed water molecules and the bending vibration of H-O-H, further confirming the presence of adsorbed water. This could be due to the high surface area of the nanocomposite, which allows for more water adsorption. Specifically, the peak at around 698 cm^{-1} can be attributed to the Ti-O-Ti stretching mode, which is a signature of anatase TiO_2 [32]. The presence of peaks in this region also suggests the successful formation of NiO and MnO_2 phases. The stretching modes for Ni-O bonds are observed around 1256 cm^{-1}, while the characteristic Mn-O vibrations, associated with γ-MnO_2 and β-MnO_2 phases, appear in the same region 718 cm^{-1}, confirming the coexistence of these metal oxides in the nanocomposite. The absence of significant peaks related to organic contaminants in the spectrum indicates the high purity of the synthesized nanocomposite.

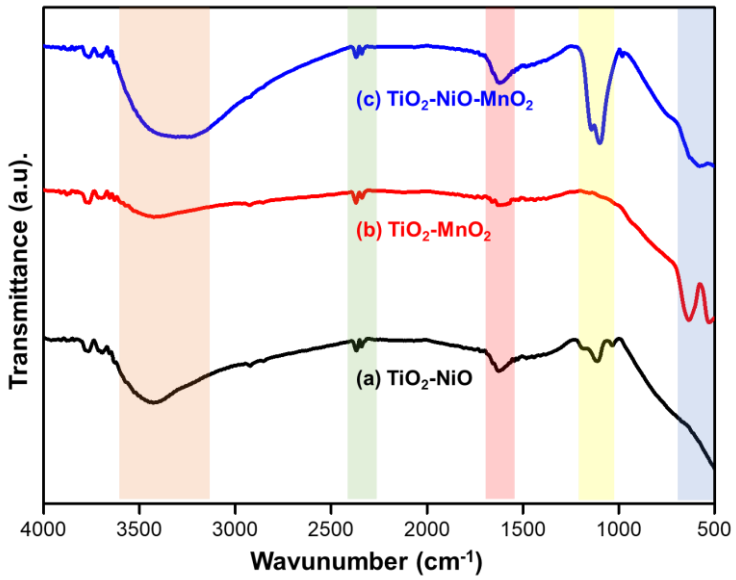

Figure 2. FT-IR spectra of (a) TiO_2-NiO, (b) TiO_2-MnO_2 and (c) TiO_2-NiO-MnO_2 nanocomposite

3.3. SEM-EDX Analysis

The morphology and elemental composition of nanocomposite were analyzed by SEM-EDX. The SEM images of the TiO_2-NiO, TiO_2-MnO_2, and TiO_2-NiO-MnO_2 nanocomposite with different magnifications are displayed in Figure 3. The SEM analysis of the three samples revealed significant morphological differences. As displayed in Figure 3(a,b), TiO_2-NiO nanocomposite is tightly packed on the surfaces and a more compact structure, with particles tightly bound together. The integration of NiO into TiO_2 promotes structural integrity and improves electrical conductivity, but the reduced porosity compared to both samples. It's visible also in Figure 3(b) that the NiO surface appears notably thick, with the presence of microcracks due to the excessive thickness resulting. Figure 3 (c,d) exhibits a fairly uniform nanosphere morphology, with the hollow spherical structures achieved through the calcination at 500 °C. Some fragments of particles were observed, which visibly demonstrated the formation of hollow spheres (Figure 3d). Moreover, in Figure 3 (e,f) the TNM nanocomposite exhibited a highly uniform and porous structure, characterized by well-dispersed nanoparticles across the surface [33,34]. This morphology facilitates efficient electron transfer and provides an increased surface area for electrochemical reactions, making it ideal for sensor applications. The synergy between TiO_2, NiO, and MnO_2 in this composite results in minimal particle agglomeration, which enhances conductivity and sensor sensitivity.

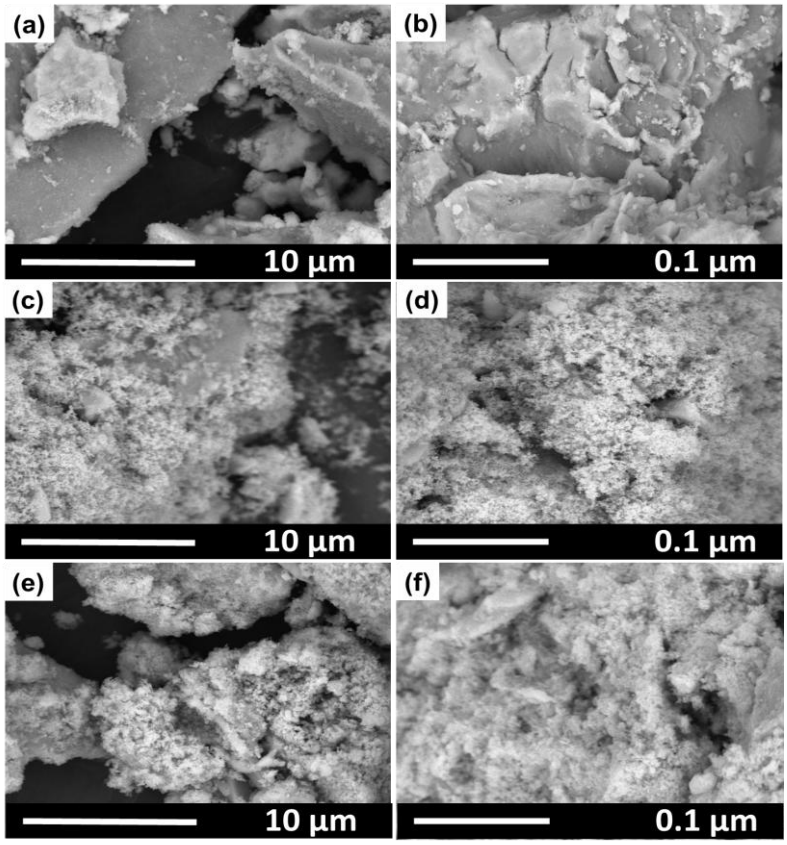

Figure 3. SEM image from (a,b) TiO_2-NiO, (c,d) TiO_2-MnO_2, and (e,f) TiO_2-NiO-MnO_2

To support this statement, the prepared nanocomposites were analyzed using EDX to determine their chemical composition both qualitatively and quantitatively. Figure 4 displays the EDX spectra for (a) TiO_2-NiO, (b) TiO-MnO_2, and (c) TiO_2-NiO-MnO_2 nanocomposite, with inset tables providing quantitative data. For TiO_2-NiO, the EDX spectrum shows peaks corresponding solely to Ti, Ni and O, with mass ratios of 12.40%, 57.60%, and 30.00%, respectively. No detectable impurities such as Na or C were observed within the EDX detection limit, indicating the high purity and well-crystallized nature of the TiO_2-NiO, consistent with the XRD results. The EDX spectrum for TiO-MnO_2, depicted in Figure 4b, reveals signals for Ti, Mn, and O, with mass ratios of 11.80%, 57.50% and 30.7% respectively. The quantitative EDX analysis of the TiO_2-NiO-MnO_2 nanocomposite, shown in Figure 4c, confirms the presence of Ti, Ni, Mn, and O with mole ratios of 7.00% for TiO_2 30.13% for NiO, 43.54% for MnO_2 and 19.31% for O, validating the successful synthesis of the TNM nanocomposite.

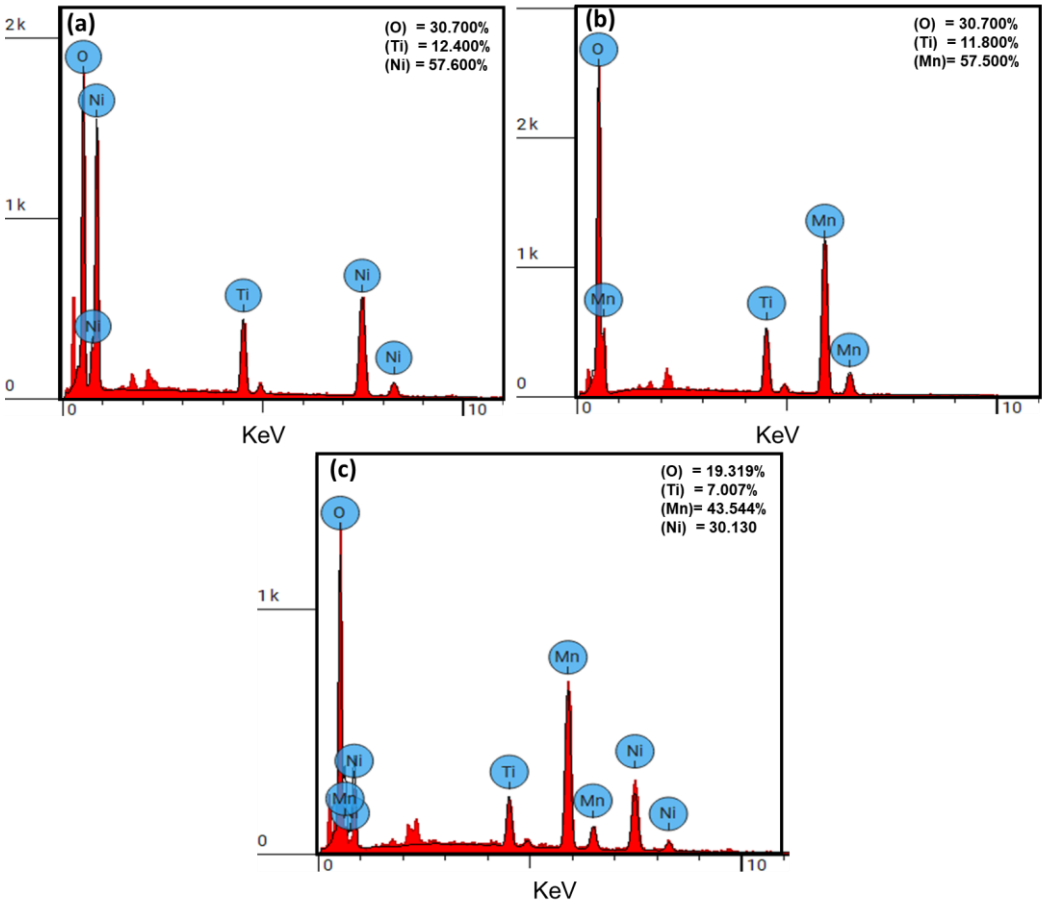

Figure 4. EDX spectra; (a) TiO_2-MnO_2, (b) TiO_2-NiO, and (c) TNM nanocomposites

3.4. Electrochemical Characterization

The CV profile of bare rGO (unmodified) exhibited a well-defined pair of redox peaks, as shown in Figure 5, displaying broad peaks in the $[Fe(CN)_6]^{3-/4-}$ solution system on its surface. The redox peaks for the rGO-TiO_2-NiO and rGO-TiO_2-MnO_2 electrodes were also observed,

both demonstrating improved electrochemical performance compared to unmodified rGO, although the enhancement in peak currents was relatively minor. It can be seen that the redox peaks of these two electrodes are nearly identical and only slightly higher than those of bare rGO, indicating that the individual contributions of NiO and MnO_2 did not result in a significant synergistic effect [35]. In Figure 5, the highest redox peak currents were observed for the rGO/TNM electrode. The oxidation and reduction peak currents increased markedly compared to the other electrodes, indicating enhanced charge transfer efficiency and redox activity. This phenomenon can be attributed to the strong synergy among the metal oxide components, which provide abundant active surface sites, thereby accelerating the electron transfer process. A comparison of the redox peak current (Ip) values for both oxidation and reduction processes across all tested electrodes is presented in Table 1.

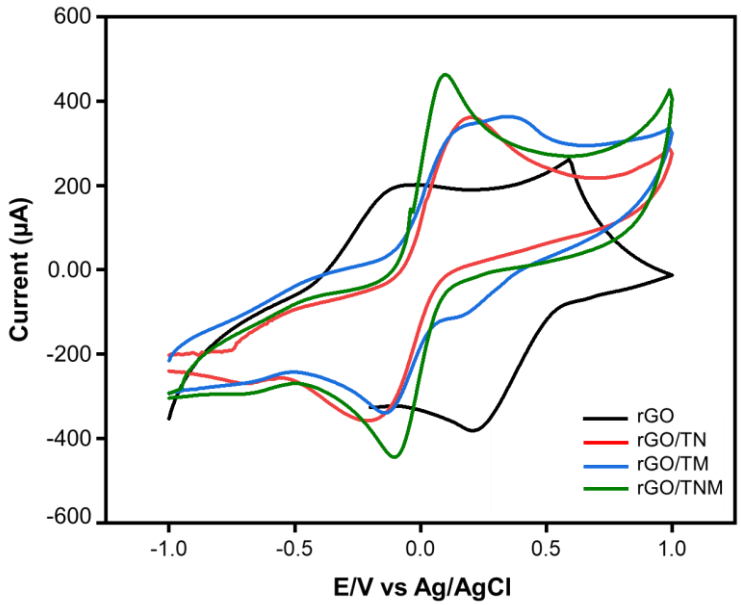

Figure 5. Voltammogram of rGO/TNM electrode with scan rate 0.1 V/s in 0.01 M $Fe(CN)_6^{3-}/Fe(CN)_6^{4-}$ solution system

Table 1. Comparison of the Ip values of pristine rGO, rGO/TN, rGO/TM, and rGO/TNM electrodes in the $Fe(CN)_6^{3-}/Fe(CN)_6^{4-}$ solution system

Electrode	***Ep* (V)**		***Ip* (µA)**	
	Ep_a	Ep_c	Ip_a	Ip_c
Pristine rGO	-0.11	0.21	191	-383
rGO-TiO^2-NiO	0.18	-0.19	359	-354
rGO-TiO_2-MnO_2	0.32	-0.14	359	-341
rGO-TNM	0.10	-0.10	466	-445

Furthermore, to understand the charge transport mechanism and the electrochemical properties of the rGO/TNM electrode, scan rate variation studies were conducted using CV in

a $K_3Fe(CN)_6$ system. This study aimed to evaluate the stability and electron transfer kinetics at the electrode surface. The obtained CV curves (Figure 6a) show that the redox peak currents increase with increasing scan rates [36,37]. Figure 6b presents a good linear relationship between the anodic peak current (Ip_a) and the square root of the scan rate ($v^{1/2}$), indicating that the redox process in this system is diffusion-controlled by the $[Fe(CN)_6]^{3-}$ ions towards the electrode surface [38,39]. The linear regression equations obtained were Ip_a (y) = 1.8007x + 0.1167 and Ip_c (y) = –1.5876x – 0.1249, with corresponding correlation coefficients (R^2) of 0.9896 and 0.9897, respectively, demonstrating excellent linearity (Figure 6b).

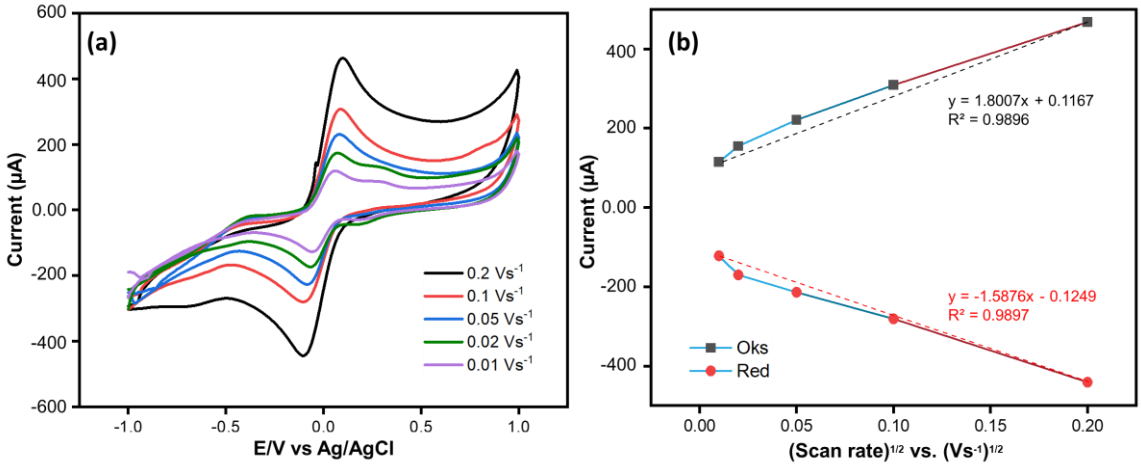

Figure 6. Voltammogram of (a) scan rate variation and (b) square root of scan rate of rGO/TNM in a $K_3[Fe(CN)_6]$

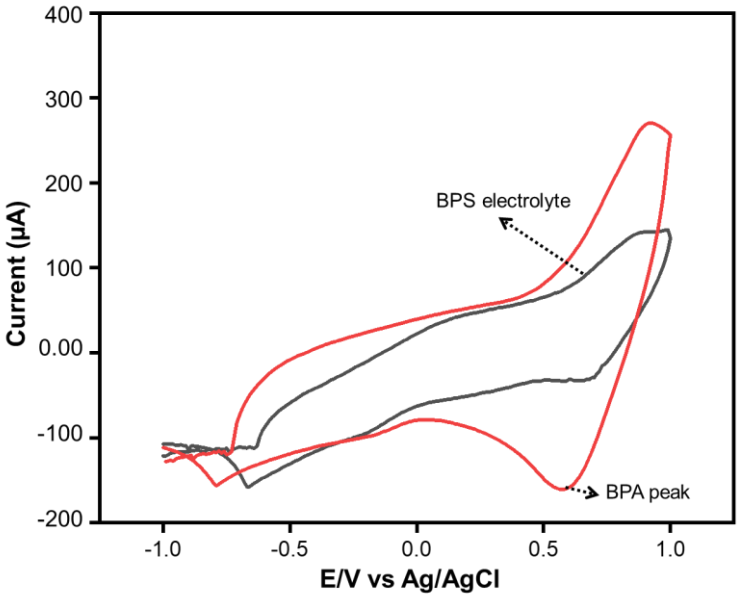

Figure 7. Voltammogram comparison of supporting electrolytes and in the presence of 1 µm BPA

3.5. Voltametric detection of BPA

In this study, the prepared rGO/TNM electrode was applied for the electrochemical detection of BPA using cyclic voltammetry. Figure 7 displays the CV curves of the rGO/TNM electrode in PBS solution containing 1.0 µg L^{-1} BPA. It is clearly observed that no distinct redox peaks appeared for the blank PBS solution (black curve), whereas after the addition of 1.0 µg L^{-1} BPA, a noticeable reduction current corresponding to BPA was observed (red curve). Additionally, the reduction mechanism of BPA in this study likely involves the conversion of the oxidized quinone-like intermediate (formed during previous oxidation) back to its hydroquinone or phenolic form. The appearance of a distinct cathodic peak in the CV curve supports this reductive transformation under the applied potential. This phenomenon indicates that the detected peak is indeed attributed to BPA, suggesting that the rGO/TNM electrode has strong potential for BPA detection. The excellent conductivity and large surface area of rGO/TNM contribute to the clear and well-defined reduction peak as expected.

Furthermore, the current response of BPA solutions with varying concentrations (0.1-1.0 µg.L^{-1}) was analyzed using the rGO/TNM electrode via CV technique. Figure 8a presents the CV curves for BPA solutions at different concentrations under optimized conditions.

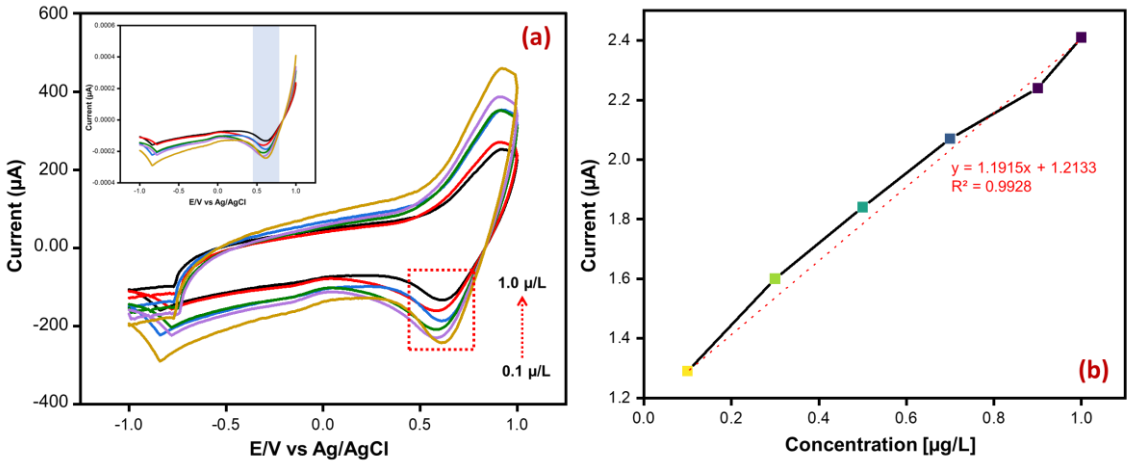

Figure 8. (a) Cyclic voltammogram of variations in BPA concentration and (b) linearity curve of BPA detection using rGO/TNM

It can be observed that the reduction peak current of BPA gradually increases with increasing BPA concentration, indicating a stable and sensitive electrochemical response. A strong linear relationship between the peak current and BPA concentration was established, with a regression equation of $y = 1.1915x + 1.2133$ and a determination coefficient (R^2) of 0.9928. The calculated limit of detection (LOD) was 0.01094 µg.L^{-1}, demonstrating the high sensitivity of the sensor. This enhanced performance can be attributed to the synergistic effects of the large specific surface area and excellent electrical conductivity of rGO, combined with the catalytic activity of the TNM nanocomposite, which collectively accelerate electron

transfer kinetics [40,41]. These findings confirm that the rGO/TNM-based electrode offers a highly promising electrochemical platform for sensitive BPA detection. Additionally, the sensor performance was compared with various previously reported sensors, as summarized in Table 2.

Table 2. Comparison of the rGO/TNM modified electrode for BPA determination with other modified electrodes

Modified Electrode	Linear Range	LOD	Analytical Methods	Ref.
CPE/TiO_2 NRs	6×10^{-4}-10^{-2} M	0.08 µM	CV	[42]
MWCNTs/$CuFe_2O_4$/GCE	10-120 µM	0.0032 µM	DPV	[43]
TiO_2/rGO-CPE	1-200 µM	0.08 µM	DPV	[21]
Gd@ZnO-MWCNTs/GCE	0.5 to 80 µM	0.2 µM	DPV	[44]
$MnFe_2O_4$/graphene/GCE	0.8-400 µmol/L	0.0235 µmol/L	CV	[45]
rGO/TNM	0.1 to 1.0 ugL^{-1} 0.439-4.39 µM	0.01094 $\mu g.L^{-1}$ 0.048 µM	CV	**This work**

4. CONCLUSION

Herein, we successfully synthesized a TNM nanocomposite and integrated it with reduced graphene oxide (rGO) to fabricate an electrochemical sensor for detection of bisphenol A (BPA). The unique combination of TiO_2, NiO, and MnO_2 nanomaterials, each contributing their catalytic and conductive properties, significantly enhanced the sensor's performance. The rGO/TNM composite electrode exhibited excellent sensitivity, selectivity, and reproducibility, making it a promising tool for detecting BPA in various environmental samples. The synergistic effects of the nanocomposite materials resulted in superior electron transfer rates and increased active surface areas, as evidenced by electrochemical measurements. This innovative sensor design offers broad potential for applications in environmental monitoring and public health, especially for rapid, low-cost detection of hazardous compounds such as BPA. Future work should focus on expanding its applicability in complex matrices and exploring further enhancements in electrode stability and lifetime.

Acknowledgments

We acknowledge the financial support from the Ministry of Education, Culture, Research and Technology of the Republic of Indonesia under the Basic Research award grant no 049/E5/PG.02.00.PL/2024 and 56/UN29.20/PG/2024 and thank the Universitas Halu Oleo for supporting this research.

Declarations of interest

The authors declare no conflict of interest in this reported work.

REFERENCES

[1] L. Barraza, Med. Ethics 41 (2013) 9.
[2] C. Xiao, L. Wang, Q. Zhou, and X. Huang, J. Hazard. Mater. 384 (2020) 121488.
[3] I.A. Kawa, Q. Fatima, S.A. Mir, H. Jeelani, S. Manzoor, and F. Rashid, Res. Rev. 15 (2021) 803.
[4] J.-H. Park, M.-S. Hwang, A. Ko, D.-H. Jeong, J.-M. Lee, G. Moon, K.-S. Lee, Y.-H. Kho, M.-K. Shin, and H.-S. Lee, Environ. Res. 150 (2016) 606.
[5] J. Il Kwak, J. Moon, D. Kim, R. Cui, and Y.-J. An, J. Hazard. Mater. 344 (2018) 390.
[6] N. Manousi, I. Priovolos, A. Kabir, K.G. Furton, V.F. Samanidou, and A. Anthemidis, Anal. Chim. Acta 1268 (2023) 341400.
[7] N.C. Maragou, N.S. Thomaidis, G.A. Theodoridis, E.N. Lampi, and M.A. Koupparis, J. Chromatogr. B 1137 (2020) 121938.
[8] L. Zhang, Y. Chen, Q. Zhu, W. Ji, and S. Zhao, Vib. Spectrosc. 113 (2021) 103225.
[9] Y. Wang, M. Wang, L. Zhou, X. Geng, Z. Xu, H. Zhang, Food Chem. 401 (2023) 134084.
[10] L.-K. Lin, and L.A. Stanciu, Sensors Actuators B 276 (2018) 222.
[11] A. Kumar, D. Singh, R. Bhandari, A.K. Malik, S. Kaur, and B. Singh, India, J. Hazard. Mater. Adv. 9 (2023) 100205.
[12] D. Wibowo, Y. Sufandy, I. Irwan, T. Azis, M. Maulidiyah, and M. Nurdin, J. Mater. Sci. Mater. Electron. (2020). https://doi.org/10.1007/s10854-020-03996-2.
[13] M. Nurdin, Z. Arham, W.O. Irna, M. Maulidiyah, K. Kurniawan, I. Irwan, and A.A. Umar, Mater. Sci. Semicond. Process. 151 (2022) 106994.
[14] M. Nurdin, M. Maulidiyah, A.H. Watoni, A. Armawansa, L.O.A. Salim, Z. Arham, D. Wibowo, I. Irwan, and A.A. Umar, Korean J. Chem. Eng. 39 (2022) 209.
[15] K.S. Yunita, I. Irwan, and T. Nakai, Surf. Eng. Appl. Electrochem. 59 (2023) 764.
[16] M. Nurdin, O.A. Prabowo, Z. Arham, D. Wibowo, M. Maulidiyah, S.K.M. Saad, and A.A. Umar, Surfaces and Interfaces 16 (2019) 108.
[17] M. Nurdin, L. Agusu, A.A.M. Putra, M. Maulidiyah, Z. Arham, D. Wibowo, M.Z. Muzakkar, and A.A. Umar, J. Phys. Chem. Solids 131 (2019) 104.
[18] M. Nurdin, M. Maulidiyah, L.O.A. Salim, M.Z. Muzakkar, and A.A. Umar, Microchem. J. 145 (2018) 756.
[19] J. Zhu, X. Huang, and W. Song, ACS Nano 15 (2021) 18708.
[20] S.W. Njoroge, P.M. Guto, I.N. Michira, and D.A. Abong'o, Anal. Bioanal. Electrochem. 16 (2024) 711.
[21] R. Hidayat, S. Wahyuningsih, and G. Fadillah, Mater. Sci. Eng. B 286 (2022) 116083.
[22] J.A. Buledi, H. Shaikh, A.R. Solangi, A. Mallah, Z.-H. Shah, M.M. Khan, A.L. Sanati,

H. Karimi-Maleh, C. Karaman, and M.B. Camarada, Ind. Eng. Chem. Res. 62 (2023) 4754.

[23] J. Lou, W. Wang, L. Yan, C. Ruan, X. Sun, W. Sun, and P. Li, Int. J. Environ. Anal. Chem. 95 (2015) 911.

[24] P. Nasehi, M.S. Moghaddam, N. Rezaei-savadkouhi, M. Alizadeh, M.N. Yazdani, and H. Agheli, J. Food Meas. Charact. 16 (2022) 2440.

[25] I. Irwan, R. Rahmin, N. Dali, N. Nohong, R. Ratna, T. Azis, A. Alimin, and M.Z. Muzakkar, Letters in Applied NanoBioScience 14 (2025).

[26] X. Wei, G. Zhu, and J. Fang, J. Chen, Int. J. Photoenergy 2013 (2013) 726872.

[27] L. Cuéllar-Herrera, E. Arce-Estrada, A. Romero-Serrano, J. Ortiz-Landeros, R. Cabrera-Sierra, C. Tirado-López, A. Hernández-Ramírez, and J. López-Rodríguez, J. Electron. Mater. 50 (2021) 5577.

[28] Y. Long, X. Zhang, M. Zhu, X. Gao, Z. Liu, S. Chen, and J. Pang, J. Energy Storage 103 (2024) 114328.

[29] J. Yang, S. Ren, B. Su, Y. Zhou, G. Hu, L. Jiang, J. Cao, W. Liu, L. Yao, and M. Kong, Catal. Letters 151 (2021) 2964.

[30] J. Gupta, A.S. Ahmed, and A. Azam, Phys. E Low-Dimensional Syst. Nanostructures 165 (2025) 116121.

[31] J. Ahmad, K. Majid, and M.A. Dar, Appl. Surf. Sci. 457 (2018) 417.

[32] Z. Arham, A.K. Ramli, M. Nurdin, and M. Natsir, Anal. Bioanal. Electrochem. 15 (2023) 711.

[33] Y. Varun, H. Augustus, N. Panda, I. Sreedhar, and S.A. Singh, Int. J. Environ. Sci. Technol. 20 (2023) 3023.

[34] B.S. Harisha, B. Akkinepally, J. Shim, and J. Lim, J. Energy Storage 87 (2024) 111466.

[35] F. Arham, Z. Arham, K. Kurniawan, M. Maulidiyah, A. Alimin, N. Dali, A. Aladin, and M. Nurdin, Sens. Imaging 26 (2025) 1.

[36] K. Kusdin, F. Mustapa, and I. Irwan, Anal. Bioanal. Electrochem. 16 (2024) 1012.

[37] Z. Arham, and K. Kurniawan, Korean J. Chem. Eng. 39 (2022) 1333.

[38] L.O.A. Salim, P. Taba, M. Zakir, and M. Nurdin, Bionanoscience 15 (2025) 110.

[39] P. Taba, M. Zakir, M. Nurdin, A.W. Wahab, D. Tahir, S. Fauziah, and A.A. Umar, Environ. Nanotechnology, Monit. Manag. (2025) 101067.

[40] Z. Arham, K. Kurniawan, and L. Anhusadar, Mater. Sci. Semicond. Process. 160 (2023) 107466.

[41] I. Ismaun, H. Halmuniati, B. Balda, I. Irwan, and Z. Arham, Surf. Eng. Appl. Electrochem. 60 (2024) 752.

[42] G. Fadillah, S. Triana, U. Chasanah, and T.A. Saleh, Sens. Bio-Sensing Res. 30 (2020) 100391.

[43] M. Baghayeri, A. Amiri, M. Fayazi, M. Nodehi, and A. Esmaeelnia, Mater. Chem. Phys.

261 (2021) 124247.

[44] S. Agrahari, A.K. Singh, R.K. Gautam, and I. Tiwari, J. Appl. Electrochem. 53 (2023) 345.

[45] S. Gao, J. Tang, L. Xiang, and J. Long, J. Cent. South Univ. 31 (2024) 1856.